On the implicit large eddy simulations of homogeneous decaying turbulence

Ben Thornber, Andrew Mosedale, Dimitris Drikakis *

*Fluid Mechanics and Computational Science Group, Aerospace Sciences Department, Cranfield University,
Cranfield MK43 0AL, United Kingdom*

Abstract

Simulations of homogeneous decaying turbulence (HDT) in a periodic cube have been used to examine in a detailed and quantitative manner the behaviour of high-resolution and high-order methods in implicit large eddy simulation. Computations have been conducted at grid resolutions from 32^3 to 256^3 for seven different high-resolution methods ranging from second-order to ninth-order spatial accuracy. The growth of the large scales, and dissipation of kinetic energy is captured well at resolutions greater than 32^3, or when using numerical methods of higher than third-order accuracy. Velocity increment probability distribution functions (PDFs) match experimental results very well for MUSCL methods, whereas WENO methods have lower intermittency. All pressure PDFs are essentially Gaussian, indicating a partial decoupling of pressure and vorticity fields. The kinetic energy spectra and effective numerical filter show that all schemes are too dissipative at high wave numbers. Evaluating the numerical viscosity as a spectral eddy viscosity shows good qualitative agreement with theory, however if the effective cut-off wave number is chosen above $k_{max}/2$ then dissipation is higher than the theoretical solution. The fifth and higher-order methods give results approximately equivalent to the lower order methods at double the grid resolution, making them computationally more efficient.
© 2007 Elsevier Inc. All rights reserved.

1. Introduction

As current computational power does not allow direct numerical simulation (DNS) of complex flows, LES has emerged as a viable alternative where the time dependent behaviour of the flow must be resolved. Conventional LES, where an explicit subgrid model is added to the averaged Navier–Stokes equations, has been employed successfully in many prototype flows, however it is known to provide excessive dissipation in flows

* Corresponding author. Tel.: +44 1234 754796; fax: +44 1234 758207.
  E-mail address: d.drikakis@cranfield.ac.uk (D. Drikakis).

where the growth of an initially small perturbation to fully turbulent flow must be resolved [1,2]. It has been recognised that some numerical schemes gain good results in complex flows without the explicit addition of a subgrid model [1]. This occurs when the subgrid model is implicitly designed into the limiting method of the numerical scheme, based on the observation that an upwind numerical scheme can be rewritten as a central scheme plus a dissipative term (see [3–5] and references therein). Such implicit subgrid models fall into the class of structural models, as there is no assumed form of the nature of the subgrid flow thus the subgrid model is entirely determined by the structure of the resolved flow [6].

Using implicit LES (or ILES), excellent results have been gained in simulation of flows as varied as Rayleigh–Taylor and Richtmyer–Meshkov instability [7,8], Free jets [9,10], channel flow [10], open cavity flow [11,3], geophysical flows [12,13], delta wings [14] and decaying turbulence [15–20]. Attempts to formalise the development of ILES numerical schemes is hindered by the inherent complexity of theoretical analysis of non-linear schemes, however, recent developments show some good agreements between truncation errors due to the numerical scheme and the required form of the subgrid terms [21,5].

Several of these flows are of mixed compressible and incompressible nature, where a compressible method is required to capture certain flow features (e.g. shock waves), yet the turbulent vortices are near-incompressible. In experimental studies [22] the turbulent Mach number rarely exceeds 0.2. Thus it is of importance to assess the performance of Godunov-type schemes applied to low Mach number turbulence.

This paper assesses the performance of high-order Godunov-type methods for these applications, via simulations of low Mach number homogeneous decaying turbulence. The study does not intend to prove that ILES is a better approach than standard LES, based on explicit subgrid scale models, for the flow in question. It is intended as a starting point for future development by identifying quantitatively the strengths and weaknesses of high-resolution methods used in ILES by comparing the ILES results with experimental studies, DNS and previous conventional LES. It is a complementary extension of the work of Garnier et al. [23], where the ability of shock-capturing schemes was tested for resolutions up to 128^3 and for six extrapolation methods from second to fifth-order. The authors concluded that the dissipation rate of the ILES methods is too high, and that the behaviour of the schemes is more akin to a low Reynolds DNS than an LES. In the present paper, the extrapolation methods employed are less diffusive and range from MUSCL second-order through to WENO ninth-order accurate. These are finite volume methods which differ in behaviour from the finite difference and flux limiting methods employed in [23]. Each of these extrapolation methods have been run on grids from 32^3 to 256^3 to examine the behaviour and convergence (if any) of turbulent statistics and spectra.

The layout of the paper is as follows. Section 2 details the numerical scheme employed, the form of the implicit subgrid model, and the method used to initialise a homogeneous, isotropic turbulent field. The effect of non-zero compressibility in the flow field is discussed. Section 3 compares the quantitative behaviour of the seven ILES variants in terms of fundamental properties of a turbulent flow field; growth of the integral length scale; decay rate of turbulent kinetic energy; time variation of enstrophy; skewness and flatness of the velocity derivative; velocity increment and pressure fluctuation probability distribution functions; kinetic energy spectra; effective numerical filter and spectral numerical viscosity. Section 4 concludes this paper and discusses the areas for future development.

2. Simulation details

2.1. Governing equations

For all simulations in this paper it is considered that the Kolmogorov scale is significantly smaller that the mesh size, equivalent to stating that the viscous effects are negligible. Therefore, the Reynolds number $Re = \infty$ and the Navier–Stokes equations reduce to the Euler equations. The three-dimensional compressible Euler equations can be written in conservative variables and Cartesian co-ordinates as

$$\frac{\partial \mathbf{U}}{\partial t} + \frac{\partial \mathbf{E}}{\partial x} + \frac{\partial \mathbf{F}}{\partial y} + \frac{\partial \mathbf{G}}{\partial z} = 0, \tag{1}$$

where

$$\mathbf{U} = [\rho, \rho u, \rho v, \rho w, e]^{\mathrm{T}}, \tag{2}$$

$$\mathbf{E} = [\rho u, \rho u^2 + p, \rho uv, \rho uw, (e + p)u]^{\mathrm{T}}, \tag{3}$$

$$\mathbf{F} = [\rho v, \rho uv, \rho v^2 + p, \rho vw, (e + p)v]^{\mathrm{T}}, \tag{4}$$

$$\mathbf{G} = [\rho w, \rho uw, \rho vw, \rho w^2 + p, (e + p)w]^{\mathrm{T}}, \tag{5}$$

$$e = \rho i + 0.5\rho(u^2 + v^2 + w^2), \tag{6}$$

and ρ, i, u, v, w are the density, specific internal energy per unit volume and Cartesian velocity components, respectively. The system of equations is completed with the specification of an equation of state for an ideal gas

$$p = \rho i(\gamma - 1), \tag{7}$$

where γ is the ratio of specific heats.

2.2. Numerical scheme

The computations were carried out using a finite volume Godunov-type method. The flux terms are evaluated by a characteristics-based Riemann solver [24]. TVD timestepping is required for the WENO schemes to retain numericaL stability, thus time advancement is achieved using a third-order TVD Runge–Kutta method [25]. Simulations using both the TVD time-stepping and third-order extended stability Runge–Kutta [25] with MUSCL limiters show that the kinetic energy decay exponent and mean velocity derivative moments up to sixth-order vary by less than 1%. This is expected as the CFL condition ensures that the time step is significantly smaller than the spatial step.

Higher-order spatial accuracy is achieved using van Leer's MUSCL limiting technique [26], or weighted essentially non-oscillatory (WENO) methods [27]. These numerical methods ensure stability by producing a vanishing viscosity solution, i.e. the numerics add dissipation which disappears in the limit of mesh size and time step tending to zero (to remain consistent with the governing equations). The full range of extrapolation methods used are

- *MUSCL* second-order: Minmod (MM), van Leer (VL) and van Albada (VA) ([28,4] and references therein),
- A new MUSCL third-order method (M3),
- MUSCL fifth-order (M5) [29],
- WENO: fifth and ninth-order (W5 and W9) [27].

For MUSCL extrapolation, the left and right states of the conservative variables at the cell faces are computed as

$$U_{i+1/2}^{\mathrm{L}} = U_i + \frac{1}{4}\left[(1-k)\phi(r^{\mathrm{L}})(U_i - U_{i-1}) + (1+k)\phi\left(\frac{1}{r^{\mathrm{L}}}\right)(U_{i+1} - U_i)\right], \tag{8}$$

$$U_{i+1/2}^{\mathrm{R}} = U_{i+1} - \frac{1}{4}\left[(1-k)\phi(r^{\mathrm{R}})(U_{i+2} - U_{i+1}) + (1+k)\phi\left(\frac{1}{r^{\mathrm{R}}}\right)(U_{i+1} - U_i)\right], \tag{9}$$

where U is the vector of cell averaged conserved variables, k is a free parameter which is set to 1/3 for the third-order limiter, and the cells are labelled by the integer i. It should be noted that the parameter k does not influence the accuracy of the second-order limiters considered here as they are symmetric (See Appendix A for the definition of this criteria). Also,

$$r_i^{\mathrm{L}} = \frac{U_{i+1} - U_i}{U_i - U_{i-1}}, \tag{10}$$

$$r_i^{\mathrm{R}} = \frac{U_{i+1} - U_i}{U_{i+2} - U_{i+1}}. \tag{11}$$

In this study the following limiters are considered

$$\phi_{\mathrm{MM}} = \min(1, r), \tag{12}$$

$$\phi_{\mathrm{VA}} = \frac{r(1+r)}{1+r^2}, \tag{13}$$

$$\phi_{\mathrm{VL}} = \frac{2r}{1+r}, \tag{14}$$

$$\phi_{\mathrm{M3}} = 1 - \left(1 + \frac{2Nr}{1+r^2}\right)\left(1 - \frac{2r}{1+r^2}\right)^N, \tag{15}$$

where VA is van Albada, VL van Leer, MM Minmod and M3 is a third-order limiter [30]. M3 includes a 'steepening' parameter N to improve the resolution of discontinuities, in this paper $N = 2$. All of the above limiters are constrained in the normal fashion to first-order accuracy at local maxima and minima. The fifth-order MUSCL scheme (M5) is slightly more complex [29]

$$\phi_{\mathrm{M5,L}} = \frac{-2/r_{i-1}^{\mathrm{L}} + 11 + 24r_i^{\mathrm{L}} - 3r_i^{\mathrm{L}}r_{i+1}^{\mathrm{L}}}{30}, \tag{16}$$

$$\phi_{\mathrm{M5,R}} = \frac{-2/r_{i+2}^{\mathrm{R}} + 11 + 24r_{i+1}^{\mathrm{R}} - 3r_{i+1}^{\mathrm{R}}r_i^{\mathrm{R}}}{30}, \tag{17}$$

where monotonicity is maintained by limiting the above extrapolations using

$$\phi_{\mathrm{M5,L}} = \max(0, \min(2, 2r_i^{\mathrm{L}}, \phi_{\mathrm{M5,L}})), \tag{18}$$

$$\phi_{\mathrm{M5,R}} = \max(0, \min(2, 2r_i^{\mathrm{R}}, \phi_{\mathrm{M5,R}})). \tag{19}$$

WENO [27,31–33] is an extension of the original ENO concept first proposed by Harten et al. [34]. It is an arguably simpler, more efficient, robust and accurate approach. For a given order of accuracy the requisite polynomial is interpolated over each support stencil that includes the interface in question. The smoothness of these candidate polynomials is then assessed in such a way that a weighted convex combination of all the resulting interface values can be obtained with minimal spurious oscillations. In effect, stencils that cross a discontinuity will be assigned a near zero weight in comparison with those that do not. By including all the stencils, the order of accuracy of the reconstruction in smooth regions of the flow increases to $2r - 1$ for polynomial reconstructions of rth order accuracy.

By way of example the third-order WENO reconstruction is presented, which derives from linear interpolation ($r = 2$). For the left-hand interface value $U_{i+\frac{1}{2},\mathrm{L}}$ there are two stencils, (x_{i-1}, x_i) and (x_i, x_{i+1}). For each stencil, the interpolation polynomial is given by

$$P^-(x) = U_i + \frac{U_i - U_{i-1}}{\Delta x}(x - x_i), \tag{20}$$

$$P^+(x) = U_i + \frac{U_{i+1} - U_i}{\Delta x}(x - x_i). \tag{21}$$

The convex combination is then given by

$$U_{i+\frac{1}{2}} = \frac{a_0}{a_0 + a_1}P^-(x_{i+1/2}) + \frac{a_1}{a_0 + a_1}P^+(x_{i+1/2}), \tag{22}$$

$$a_0 = \frac{C_0}{(\epsilon + (IS)^-)^2}, \quad a_1 = \frac{C_1}{(\epsilon + (IS)^+)^2}, \tag{23}$$

where the coefficients C_k are determined for optimal weighting and the smoothness indicators (IS) are given by $(IS)^- = (U_i - U_{i-1})^2$ and $(IS)^+ = (U_{i+1} - U_i)^2$. Finally, ϵ is a small number used to prevent divisions by zero in a perfectly smooth flow. The equations for fifth and ninth-order methods are naturally more complex but the principle is the same [27].

Regarding the CPU time taken to complete the very high order accuracy simulations, the ratio of CPU times to that required to carry out the second-order van Leer simulations is 1.2 for M5 and W5, and 2.5 for W9. This does not include communication times for parallel computations as these depend on the hardware used and the number of parallel blocks utilised. This was not significant for the number of processors employed (maximum of 96 AMD Athlon processors used for the 256^3 simulations).

2.3. Implicit subgrid models

ILES is a so-called 'no model' turbulence model. It is assumed that the numerics provide sufficient modelling of the subgrid terms to allow the 'correct' dissipation of turbulent kinetic energy. As pointed out in the introduction, the subgrid model embedded in the numerical method used to discretise the convective terms is determined entirely by the structure of the flow. This has obvious benefits in the simulation of transitional flows where excess dissipation can damp the growth of critical modes. A detailed description of the implicit subgrid model would be too lengthy to include within this paper (see, for example [4,21,9,35,5]), however an outline of the components of the ILES model will be given in this section.

The finite volume fluxes for the Godunov method can be written in the following format [28]:

$$\mathbf{F_{i+1/2}} = \frac{1}{2}(\mathbf{F_L} + \mathbf{F_R}) - \frac{1}{2}|\mathbf{A}|(\mathbf{U_R} - \mathbf{U_L}), \tag{24}$$

where

$$|\mathbf{A}| = \mathbf{K}|\mathbf{\Lambda}|\mathbf{K}^{-1}, \tag{25}$$

is the flux Jacobian, $\mathbf{\Lambda}$ is a diagonal array of eigenvalues, $\mathbf{F}$ is the vector of fluxes and the subscripts R and L indicate the right and left side of the interface, respectively. Using this expression it can be seen that the influence of the extrapolation method on the kinetic energy dissipation rate can be understood as the combination of two effects.

The first term on the right-hand side of (24) is directly computed from the extrapolated quantities thus it is an approximation of the flux to a certain order of accuracy. In finite volume methods the filtered quantity is inverted to recover the continuous function to estimate the extrapolated cell interface values. The numerical grid is assumed to be equivalent to a top hat filter in physical space, i.e.

$$\overline{U} = \frac{1}{\Delta V} \int_0^{\Delta v} U \Delta V, \tag{26}$$

where $\overline{U}$ indicates the cell averaged quantity, and $\Delta V = \Delta x \Delta y \Delta z$. The inversion is usually done using a Taylor series expansion of the top hat filter, and shows that the leading order difference between the cell averaged quantity and continuous function measured at the cell centre are at second-order, i.e. in one dimension (for more details see [6,21,36])

$$U = \overline{U} - \frac{\Delta x^2}{24}\overline{U}_{xx} + \mathcal{O}\Delta x^4, \tag{27}$$

where $(.)_x$ indicates a derivative with respect to x. In the construction of schemes with accuracy higher than second-order, this conversion has to be taken into account in the design of the scheme. This implies that higher-order schemes inherently include some leading order influences of the subgrid variations for the resolved modes (either turbulent or laminar variations). For example, at third-order accuracy the leading order kinetic energy dissipation term can be determined from modified equation analysis (MEA) following the methodology in [37,21]. The first step in this process is to write the extrapolated quantities as a function of the cell averaged quantity, expanding the interface value in a Taylor series as is done when deriving truncation terms for the linear advection equation. Next, subtract the exact Euler equations and gather together the leading order terms in powers of Δx, Δy and Δz. These remaining terms form the truncation error. As an example, taking third-order accurate extrapolated quantities, the leading order terms can be written as the divergence of a tensor τ. In two dimensions

$$\tau^{xx} = -\frac{\Delta x^2}{12}u_x^2 - \frac{\Delta y^2}{12}u_y^2, \tag{28}$$

$$\tau^{xy} = \tau^{yx} = -\frac{\Delta x^2}{12}u_x v_x - \frac{\Delta y^2}{12}u_y v_y, \tag{29}$$

$$\tau^{yy} = -\frac{\Delta x^2}{12}v_x^2 - \frac{\Delta y^2}{12}v_y^2. \tag{30}$$

An equivalent results is also achieved through Approximate Deconvolution, as detailed in [36,6]. The dissipation of kinetic energy due to this stress tensor is

$$\frac{\mathrm{d}E_D}{\mathrm{d}t} = -\int_D (u_x \tau^{xx} + u_y \tau^{xy} + v_x \tau^{yx} + v_y \tau^{yy}) \mathrm{D}X\,\mathrm{D}Y, \tag{31}$$

where E_D now indicates the kinetic energy in a domain of size $\mathrm{D}X\mathrm{D}Y$ without external forces. This gives

$$\frac{\mathrm{d}KE}{\mathrm{d}t} = \frac{\Delta x^2}{12}\left[\langle u_x^3 \rangle + \langle u_x u_y v_x \rangle\right] + \frac{\Delta y^2}{12}\left[\langle v_y^3 \rangle + \langle u_y v_x v_y \rangle\right]. \tag{32}$$

The leading order terms are proportional to the skewness of the velocity derivative, which is negative in turbulent flows thus providing dissipation of resolved kinetic energy. Naturally, higher-order extrapolation methods will approximate the subgrid variations to a higher order of accuracy for modes which can be resolved on a given grid.

The extrapolation method also influences the second term in (24) through the difference of the left and right extrapolated quantities. Ideally this should remove the kinetic energy from the system in a form similar to the action of subgrid vortices on the resolved vortices. Kolmogorov proposed the following similarity hypothesis [38,39]

$$r\bar{\epsilon}_r = \frac{5}{4}\overline{\Delta u^3} \tag{33}$$

where $\bar{\epsilon}_r$ is the dissipation rate averaged over the distance r, and Δu is the velocity increment. This represents the dissipation due to homogeneous isotropic turbulence per unit time per unit area. It has been shown to be valid for Taylor–Reynolds numbers greater than 1000 and when the length scale r lies within the inertial range [40].

The only time that kinetic energy is irreversibly changed into heat in the solution of a Riemann problem is between a shock wave and contact surface. All other flow features are isentropic. As determined in [41,42] the entropy change ΔS due to the passage of a shock wave can be written as

$$\Delta S = -\frac{\partial^2 p}{\partial V^2}\bigg|_S \frac{\Delta V^3}{12T}, \tag{34}$$

where V is the specific volume, p is the pressure, and T is the temperature. Using the Hugoniot relations and under the assumption of a perfect gas this can be written as

$$T\Delta S = -\frac{(\gamma + 1)}{12a}\Delta u_s^3 \tag{35}$$

where γ is the ratio of specific heats, a is the sound speed, and Δu_s is the velocity jump over the shock wave. This gives a measure of the irreversible dissipation of kinetic energy in the Riemann solution, an increase of specific internal energy at the cost of specific kinetic energy. Thus at an interface where the solution of a Riemann problem lies between the contact surface and shock wave there will be an effective dissipation of kinetic energy proportional to Δu_s^3 – analogous to (33). The choice of extrapolation method directly influences the magnitude of the velocity jump, thus modifying the dissipative properties of the numerical scheme.

An important implication of this is that the differences between the extrapolated quantities (i.e. $U_R - U_L$) are as important as the formal order of accuracy of the extrapolation in characterising the dissipative properties of the scheme. For example, MM, VA, and VL are all second-order schemes and so should give similar results. However, the difference between the right and left extrapolated values at leading order is second-order for MM, but third-order for VA and VL. This explains the dissipative behaviour of the MM limiter as compared to the VA and VL limiting methods.

An additional component to consider is the behaviour of the extrapolation methods as regards monotonicity. MUSCL schemes are strictly monotonic, however WENO methods are not. Oscillations in one dimension are manifested as vortex breakdown in two and three dimensions. This dispersive behaviour of the very high-order methods can inject energy at the small scales, altering the kinetic energy spectrum.

Given a perfect subgrid model, an LES at several different resolutions should be identical given that the cutoff wave number lies within the inertial range. However, it is expected that the model is not perfect, thus increasing the resolution should have the effect of reducing the effects of the numerical method on a given mode, shifting it to higher wave numbers. Thus any errors induced via the subgrid model should decrease with increased resolution and order of the schemes.

The numerical methods employed here satisfy the second law of thermodynamics on a global level. It is possible that there are local decreases, however it is very difficult to quantify as it is not easy to separate local generation of entropy from the flux of entropy from neighbouring cells. An analysis of entropy generation in compressible finite volume schemes shows that at leading order local entropy generation is always positive, as long as the CFL limit is respected [43].

2.4. Initialisation

The flow field was initialised using a method derived by Youngs and utilised in previous simulations of decaying turbulence [8,7]. The flow field has an initial kinetic energy spectrum given by the analytical solution in the case of dominating viscous effects [22]:

$$E(k) = u'^2 \frac{k^4}{k_p^4} \sqrt{\frac{8}{k_p^2 \pi}} \exp(-2(k/k_p)^2), \tag{36}$$

where k is the wave number, and the peak in the energy spectrum is defined by changing the peak k_p in the exponential. Unless otherwise stated the peak of the energy spectrum was chosen at $k_p = 4$ to aid comparison with previous results from Youngs [8,7]. To ensure the generation of an almost non-divergent (i.e. incompressible) velocity field, the velocity is formed from components of a vector potential A, which satisfies the following relationship:

$$u = \nabla \times A. \tag{37}$$

As the divergence of a curl is identically equal to zero this gives a non-divergent velocity field. The vector potential is initialised with a Gaussian distribution of amplitudes and random phases which is rescaled linearly to give a velocity field satisfying

$$KE = \frac{3}{2}u^2 = 0.5, \tag{38}$$

$$M = \frac{u'}{c} = 0.1, \tag{39}$$

where u is the mean turbulent velocity. However, although this gives zero compressibility in the initial condition, the rate of change of compressibility is not necessarily zero, as has been reported by several authors [44,45,17,46,47]. The effectiveness of this method was investigated by decomposing the compressible and incompressible velocity fields in Fourier space using the Helmholtz decomposition. This splits an arbitrary vector into solenoidal (i.e. incompressible) and dilational (compressible) components [44,45,17,46,47]. The velocity in Fourier space can be written as a sum of the solenoidal and dilational velocity components:

$$u(\mathbf{k}) = u_s(\mathbf{k}) + u_d(\mathbf{k}), \tag{40}$$

where

$$\nabla \cdot u_s(\mathbf{k}) = 0, \tag{41}$$

thus the solenoidal and dilational components can be calculated given the three-dimensional Fourier transform of the velocity field

$$u_s(\mathbf{k}) = u(\mathbf{k}) - \frac{\mathbf{k} \cdot u(\mathbf{k})}{|\mathbf{k}|^2} \mathbf{k}, \tag{42}$$

$$u_d(\mathbf{k}) = u(\mathbf{k}) - u_s(\mathbf{k}). \tag{43}$$

Fig. 1 shows the total resolved kinetic energy in the compressible and incompressible modes, respectively, for a 32^3 VL simulation. The energy in the compressible modes is about three orders of magnitude less than the energy in the incompressible modes and decreases as the simulation continues. It was found that even for Mach = 0.5 the compressible component at initialisation is less than 1%. Comparisons with previous results [44,45,17,46,47] show that the initial conditions are effectively reducing the influence of compressibility effects. A key observation of the evolution of the kinetic energy in the compressible component is that it is highly oscillatory. Kovasnay [48] showed that in the absence of viscosity and at low Mach number the vorticity, pressure and entropy are decoupled at first-order; viscosity acts to couple the pressure and entropy, but the vorticity remains decoupled. This was demonstrated via a perturbation analysis of the governing equations which show that to leading order the pressure perturbations are dominated by acoustic modes which are not related to vorticity. This partial decoupling leads to the oscillations in compressible kinetic energy at late times. The spectra shown in Fig. 2 illustrate that the energy in the compressible modes is largely restricted to the lower wave numbers. The undesirable aspect of this is that on the short time scales the rate of change of energy at low wave numbers is oscillatory and is due to the compressible modes. Due to this, the kinetic energy dissipation rate at a given point in time must be computed as an average of the rate of change centred on the time point of interest.
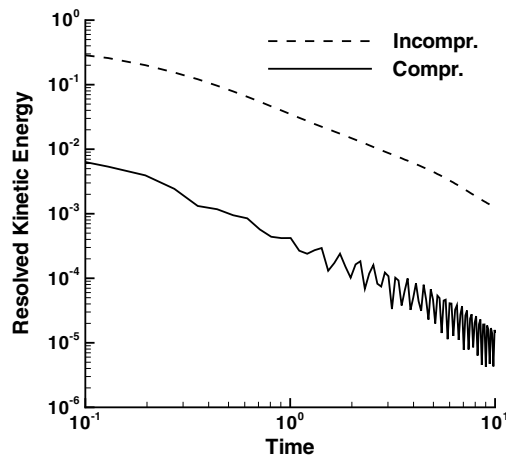

Fig. 1. The amount of kinetic energy contained in the incompressible and compressible modes in a 32^3 simulation using VL extrapolation.
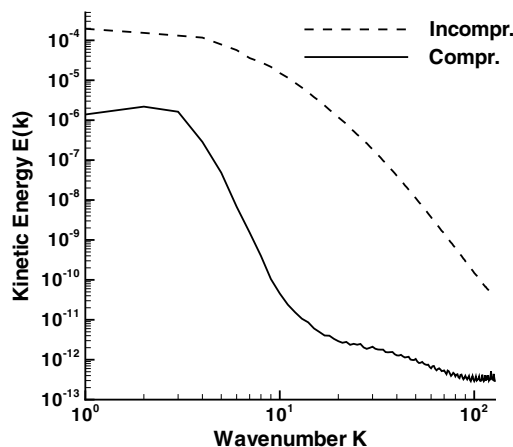

Fig. 2. The compressible and incompressible kinetic energy spectra for a 256^3 using VL extrapolation.

It should be noted that although a quasi-incompressible turbulent flow field is initialised, turbulence of mean Mach 0.1 would not be seen in an incompressible flow, indeed, it is likely that the mean flow would be highly compressible. Hinze [22] states that even at mean flow Mach number of up to 5 in strong shear layers a turbulent Mach number greater than 0.2 has never been observed.

Fig. 3 shows isosurfaces of equal vorticity magnitude taken at $t = 0$ and $t = 1$ for the 128^3 case with M5 extrapolation. This shows the initial flow field composed of low wave number modes, and the fine scale worm like vortical structures present in the fully developed turbulent flow field. The form of the structures present in the flow field does not change at later times. Fig. 4 shows the development of the skewness at each of the mesh resolutions for M5 demonstrating that a steady state is achieved after a relatively short period of time allowing for good statistical averages, especially at the higher resolutions. The simulations were run to a non-dimensional time of $t = 5$ for all mesh resolutions, corresponding to approximately 8 eddy turnover times.

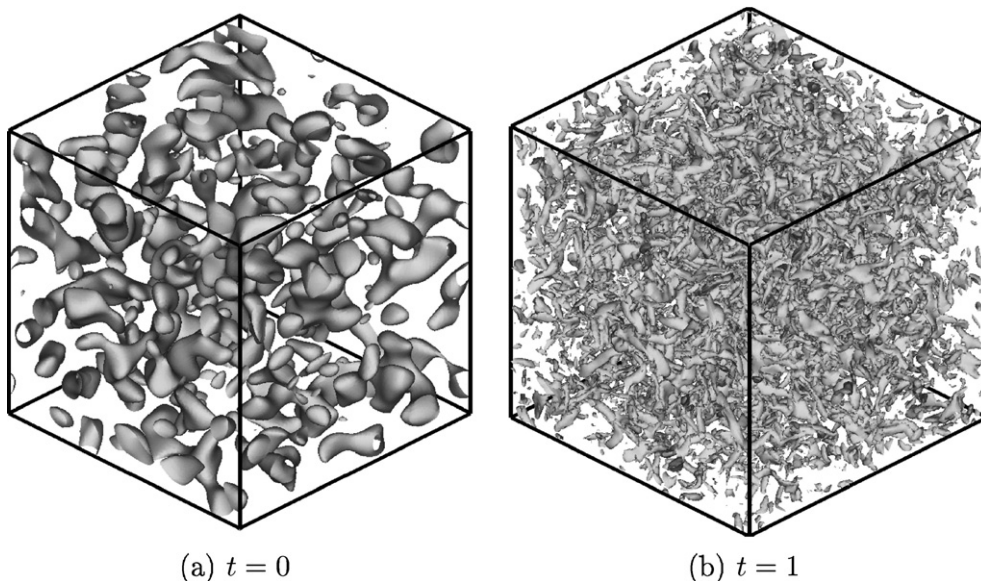(a) $t = 0$ (b) $t = 1$

Fig. 3. Iso-vorticity surfaces at $\sqrt{\omega^2} = 5$ illustrating the initial condition and fully developed homogeneous turbulence in a 128^3 using M5 extrapolation.
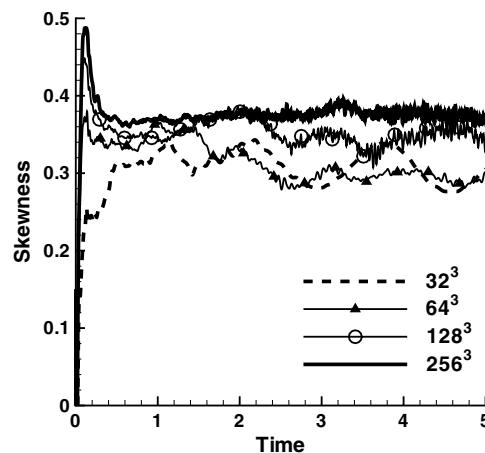

Fig. 4. Velocity derivative skewness as a function of time at several resolutions using M5 extrapolation.

3. Results and discussion

3.1. Turbulent isotropy

It is important to quantify turbulent isotropy, as turbulent theory relies on this assumption to derive analytical expressions for kinetic energy decay rates and growth of the length scales. The integral length was calculated from the longitudinal and transverse energy spectra using [49,50]

$$L_1 = \frac{\pi}{u_{\text{rms}}^2} E_{11}(k = 0), \tag{44}$$

$$L_1 = \frac{2\pi}{u_{\text{rms}}^2} E_{22}(k = 0), \tag{45}$$

where

$$E_{11}(k_1) = \frac{1}{\pi} \langle u_1^2 \rangle \int_0^\infty dx_1 f(x_1) \cos k_1 x_1, \tag{46}$$

$$E_{22}(k_1) = \frac{1}{\pi} \langle u_1^2 \rangle \int_0^\infty dx_1 g(x_1) \cos k_1 x_1, \tag{47}$$

and f and g are the second-order longitudinal and lateral correlation functions relative to the 1-direction. These are then averaged in all three directions. Both definitions of the integral length agree to within ten percent throughout the period of the simulations, however, it is observed that the simulations become increasingly more anisotropic at late times. There is a considerable anisotropy evident in the mean velocities for the 32^3, as it is extremely under-resolved. At this resolution there are only 8 cells per wavelength even at the peak of the energy spectrum. Above 32^3 the maximum mean square turbulent velocities in each direction match the mean turbulent velocity to within 6% throughout the simulation.

3.2. Kinetic energy decay rate and growth of the length scales

It is widely accepted that the evolution of kinetic energy in homogeneous isotropic turbulence can be written as follows [22]:

$$3/2u^2 = A(t - t_0)^{-p}, \tag{48}$$

where u is the root mean square turbulent velocity, A is a constant, t_0 is the virtual origin in time, and p is a positive constant. If the exponent is not in a physically realistic range then the simulations will rapidly decorrelate with reality. In addition to this, the growth of the energy containing scales, i.e. the integral length scale, must be represented accurately, as these eddies typically represent the dominating structures in the flow. The growth of the integral length scale is

$$L_1 = B(t - t_0)^q, \tag{49}$$

and q is a positive constant [51]. To facilitate comparison with conventional LES studies, the virtual origin in time $t_0 = 0$ when computing the mean kinetic energy decay exponent and growth of the integral length scales.

Fig. 5 shows the total resolved kinetic energy using the MUSCL fifth-order extrapolation method. Only resolutions of above 32^3 are shown for clarity. There is very little decay in kinetic energy in the first instant as the energy is being transferred from the low to high wave numbers. Once the high wave numbers are populated, the numerical dissipation increases until an approximately constant power law decay is seen.

Wind tunnel experiments using grid generated turbulence have measured kinetic energy decay rates $p \approx 1.2$–1.3 [52–56]. Theoretical analysis does not give a clear solution, however, it is expected that the decay should lie between $p \approx 1.2$ [57,51] and $p \approx 1.4$ [58–60]. Recent DNS at $Re_\lambda < 250$ by Ishida et al. [61] with an initial spectrum proportional to k^4 gave $p = 10/7$. The mean decay exponent p from $t = 1$ to 5 for each extrapolation method is detailed in Table 1.

At 32^3 all second and third-order methods exhibit a decay rate which is significantly less than physically expected. As will be discussed in the following section, the velocity derivative moments for these schemes
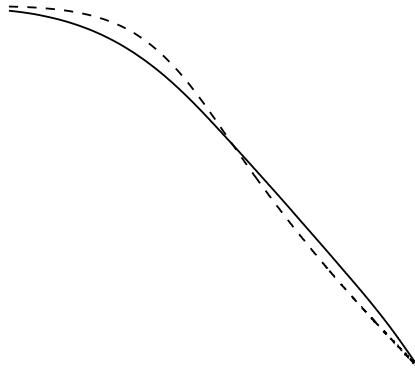
at this resolution returns rapidly to Gaussian, thus no turbulent field exists. Excessive numerical dissipation acts on the resolved modes, as even at the peak of the kinetic energy spectrum there are only 8 cells per wavelength. It should be noted that the decay rate alone cannot characterise a numerical method as the decay rate depends on the resolved features. For example, a method may have a low mean decay rate simply because all short wave perturbations have been dissipated from the system at an early time – this is the case with the Minmod limiter at 32^3.

The decay exponent for the Minmod limiter at 64^3 is in excellent agreement with the quoted value of $p = 1.3$ for 64^3 in Garnier et al. [23], thus confirming the consistency of the comparison. However, the other schemes exhibit a less diffusive behaviour. At higher resolutions, and at higher orders of accuracy, the decay exponent lies between 1.16 and 1.58 for all methods employed, whereas [23] report $p > 2$. The results here are in good agreement with the previous study by Youngs [8] which reported $p = 1.41$ using a Lagrangian based ILES code with the same initialisation method.

Compared to the experimentally determined decay exponents these results are higher, however, there is uncertainty in the choice of the virtual origin t_0 in both simulation and experiment. The ILES methods compare favourably with conventional LES, where the decay exponent $p = 1.17$–2 [62–69].

In comparing the limiters, the two fifth-order methods and W9 give the most physically realistic kinetic energy decay rates at low resolution. At all other resolutions the decay rate remains within a physically realistic range for all limiters, given the uncertainties in determining t_0.

Two additional simulations of 256^3 resolution were carried out with the Minmod limiter, where the peak of the initial energy spectrum were chosen $k_p = 1$ and 12, respectively. The two simulations differ quite significantly in flow structure and behaviour. The lower the initial peak of the spectrum, the longer the period of redistribution of energy before a power-law decay of kinetic energy begins. The average decay exponent p is 2.12 for $k_p = 1$ and 1.29 for $k_p = 12$. The theoretical decay rate of constrained turbulence (i.e. when the energy containing scales are close to the size of the box) is $p = 2$, which is in good agreement with the decay rate for the case where $k_p = 1$. This behaviour is nearly identical to that seen in the symmetry breaking
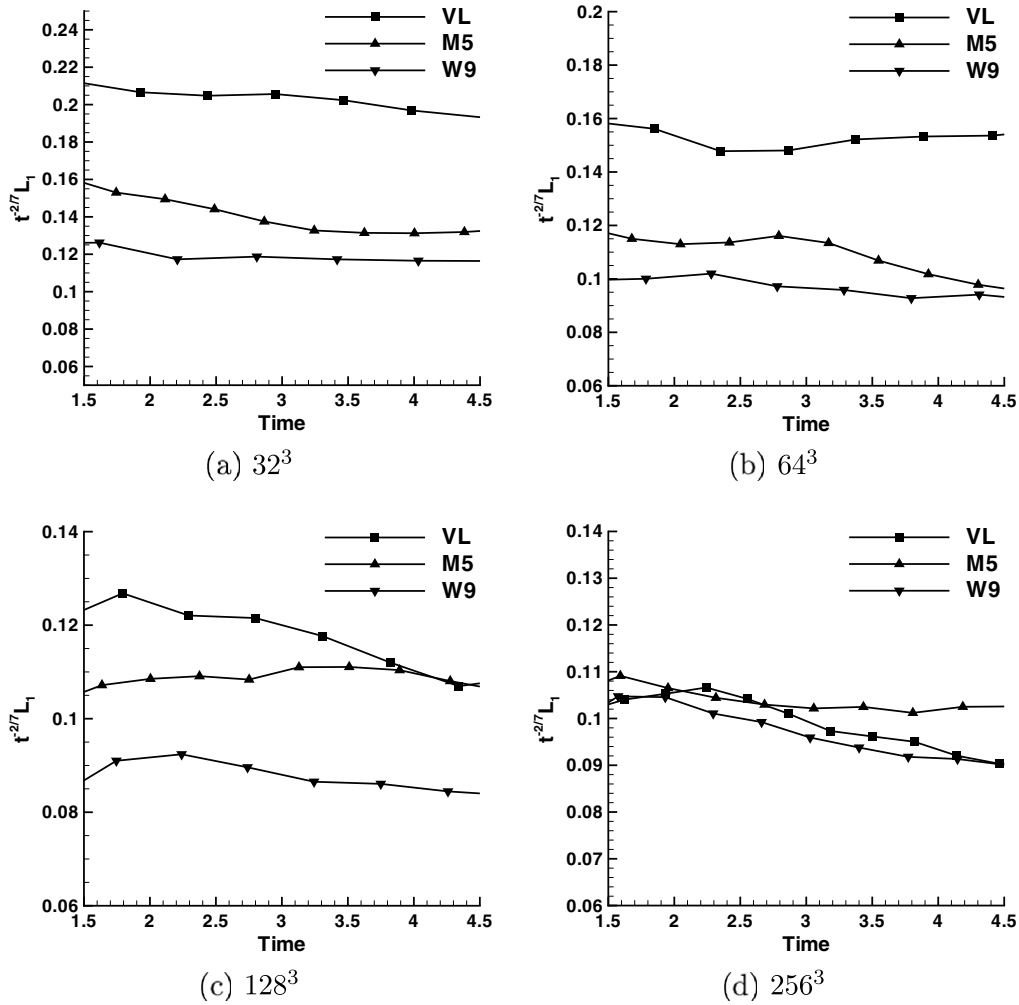
Fig. 6. Normalised integral length $t^{-2/7}L_1$ plotted against time for different resolutions.

turbulent decay of the Taylor–Green vortex, where initially large coherent structures develop instabilities and break down [15,70].

Given an initial spectrum of k^4 at low wave numbers it is expected that the integral length should grow proportional to $t^{2/7}$ [22,51], potentially moving to $t^{2/5}$ if the low wave numbers take on a k^2 form at late time. Fig. 6 shows the normalised integral length scale $t^{-2/7} L_1$ for all grid resolutions for three extrapolation methods. These plots are representative of the behaviour of all of the extrapolation methods employed in this study. The lines do not lie on top of each other as each numerical scheme has a different time origin for the decay of kinetic energy and the growth of the integral length scale. It can be seen that the integral length grows proportional to $t^{2/7}$ as expected, and that this relationship becomes more accurate as the resolution and order of the method increases.

3.3. Structure functions and enstrophy

The velocity structure functions are typically used to quantify if the flow is turbulent, and its characteristics. These are computed as [2]

$$S_n = (-1)^n \frac{\langle (\partial u/\partial x)^n \rangle}{\langle (\partial u/\partial x)^2 \rangle^{n/2}}, \tag{50}$$

where n is a positive integer, and the derivatives are computed using second-order accurate centred differences and then averaged over all three directions. The third-order velocity structure function ($n = 3$), or skewness, is directly related to enstrophy in isotropic homogenous turbulence, and the fourth-order structure function ($n = 4$), or flatness, gives a measure of the probability of occurrence of extreme or mild events. Typically, the lower the absolute value, the higher the numerical dissipation.

The flatness increases consistently with Reynolds number, at a rate approximately $S_4 \propto 3 + 1/2Re^{0.25}$. The most recent experimental results measured $S_3 = 0.34$, and $S_4 = 3.75$ for $Re_\lambda = 720$ [56], both lower than previous experiments. Computational results from previous DNS and LES simulations are summarised in Tables 2 and 3.

Table 4 details the average skewness functions in the present study, listed in approximate order of decreasing dissipative behaviour of the numerical scheme. It is expected that increasing the resolution should increase the skewness until it reaches the state expected for fully developed homogeneous decaying turbulence. Sreenivasan and Antonia [71] have compiled many experimental velocity structure function measurements. The skewness appears constant at approximately 0.5 between Reynolds 10 and 1000, but increases above this threshold. In the current study, as the mesh resolution increases, the skewness increases converging towards a value of around 0.37. This is in good agreement with the most recent experimental results of 0.34 for $Re_\lambda = 720$ [56] and previous ILES results [23], but lower than DNS results. The close agreement with the results of Kang et al. [56] is interesting as the integral length scale in the experiments is approximately 1/4 the size of the wind tunnel – and in the current simulations it is approximately 1/4 of the box size.

At the lowest resolution the skewness factor for all second and third-order limiting methods is much lower than the experimental values and tends rapidly back to a Gaussian distribution. The numerical dissipation of the scheme does not allow an adequate number of undamped modes to represent a turbulent flow field. However, at fifth-order and higher the numerical schemes capture the non-Gaussian behaviour well. As the majority of simulations around complex geometries are not well resolved this is an important point to note. As is generally accepted, Minmod is very dissipative, and not a good extrapolation method to use for turbulent flow. This is illustrated in the skewness values, which remain much lower than expected until resolutions of 128^3. At 64^3 the van Albada, van Leer and MUSCL third-order have physically realistic skewness values, close to experimental results. Surprisingly, the skewness decreases when using W9 methods, indicating that the M5 and W5 perform best at all resolutions.

The mean flatness is detailed in Table 5. Comparing the results to experimental results reported in [71] the flatness should increase consistently with Reynolds number, at a rate approximately $S_4 \propto 3 + 1/2Re^{0.25}$. This implies that the ILES simulations are achieving average Taylor–Reynolds numbers of approximately one hundred over the course of the simulation, during which the mean turbulent velocities decrease by one-fifth. However, the experiments of Kang *et al.* measured lower flatness of 3.75 at $Re_\lambda = 720$, which would give the simulations a much higher effective Re_λ within the simulations. The flatness does not change significantly with increasing resolution, or increasing order of the numerical scheme. M3 has the highest mean value at low resolution, however at higher resolutions there is little difference between the schemes. This indicates that the probability of extreme events is not increasing with increasing resolution, contradictory to expected behaviour.

Table 2
Velocity structure functions computed from DNS

Quantity	[83]	[84]	[85]	[73]	[62]	[86]	[87]	[64]	[46]	[74]
Re_λ	45	83	64	150	<51	202	168	195	175	460
S_3	0.47	0.51	0.4	0.5	0.58	0.44	0.52	0.54	0.45	0.55
S_4	–	–	4.05	5.9	4.31	–	6.1	6.7	–	7.91

Table 3
Velocity structure functions computed from LES

Quantity	[63]	[16]	[65]	[66]	[56]	Gaussian
Re_λ	∞	248	<71	∞	720	–
S_3	0.4	–	0.4	0.22	0.42	0.00
S_4	2.73	3.6	–	–	–	3.00

Table 4
Third-order velocity structure functions

Resolution	MM	VA	VL
32^3	0.08	0.11	0
64^3	0.22	0.32	
128^3	0.31	0.35	
256^3	0.34	0.37	

Table 5
Fourth-order velocity structure function

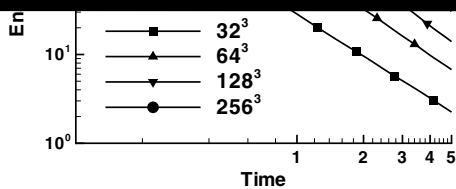| Resolution	MM
32^3	4.09
64^3	4.07
128^3	4.
256^3	

Fig. 7a) shows the time variation of the enstrophy ($\langle \omega^2 \rangle$, where ω is the vorticity) for each mesh resolution for the van Leer limiter. Fig. 7b) shows the variation with method at a 64^3 resolution. Above 128^3 resolution for the second and third-order methods, and 64^3 for the higher-order methods there are two clear stages as reported in previous studies [58,72]. In the first stage the entrophy increases due to vortex stretching which transfers energy to the smaller, faster moving vortices. Once the energy spectrum is fully developed, the ens- reduces with time as numerical dissipation decreases the resolved kinetic energy. In comparing the dif- methods, the higher the order of the method, the higher the enstrophy peak, reflecting the decreasing W9 is the least dissipative via this measure, followed by W5 and M5. W9 is equivalent to van Leer mesh resolution, whereas W5 and M5 are slightly less than double. At late times M5 has higher that setting local minima and maxima to first-order accuracy does not signif- icantly of the scheme.

3.4. Probability distribution functions

The velocity probability distribution functions (PDFs) have been computed for each grid reso- lution and method velocity increment is defined as $\delta u_i = u_i(x + \Delta x) - u(x)$. Figs. 8 and 9 show the PDFs normalised with experimental results by Kang et al. [56] taken at $Re_\lambda = 626$, and DNS by Vincent and Mene [ ] ($Re_\lambda \approx 150$) and Gotoh et al. [74] ($Re_\lambda \approx 381$). Note that the van Albada, Min-
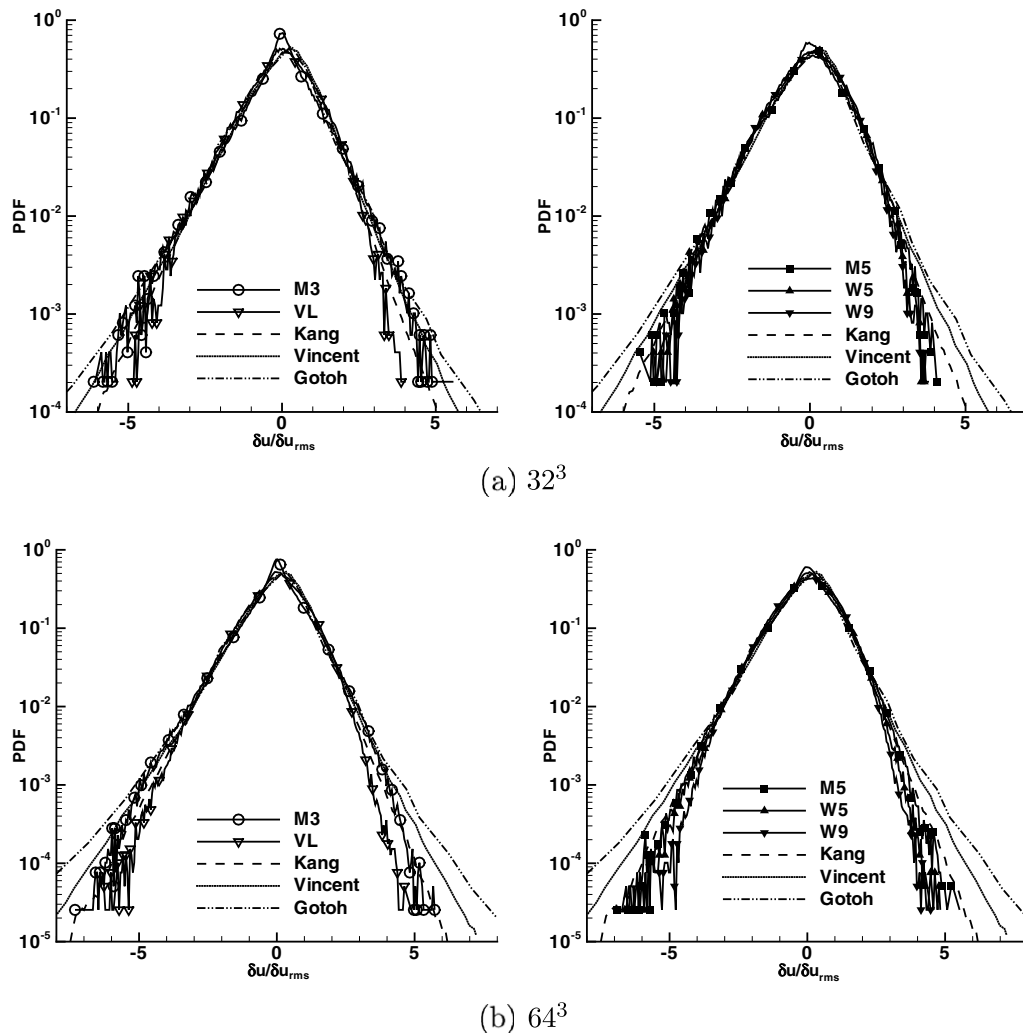
Fig. 8. Velocity increment PDFs compared to experimental results by Kang et al. [56], and DNS by Vincent and Meneguzzi [73] and Gotoh et al. [74] at $t = 2$.

mod and van Leer give very similar results hence the first two are not shown. All methods capture the non-Gaussian behaviour of the velocity increments, the fifth-order MUSCL limiter giving best agreement with the experimental results. Indeed, at 256^3 resolution the M3 and M5 limiters lie almost directly on top of the experimental results for negative increments, and follow the positive increments up to $\delta u/\delta u_{rms} = 5$. Surprisingly, the ninth-order WENO has the least activity in the wings compared to the other very high-order schemes. The van Leer, Minmod and van Albada limiters give exponential wings, but less intermittent than both experimental and DNS results.

The results shown here demonstrate that the shock capturing schemes give velocity increment PDFs in very good agreement with experimental results at $Re_\lambda \approx 626$. This appears contradictory to the results in Garnier et al. who show that the velocity increment PDFs are close to DNS results at $Re_\lambda \approx 20$. Comparing DNS of Vincent and Meneguzzi [73] and Gotoh et al. [74], and the experimental results of Kang et al. [56] it is clear that there is a large discrepancy in the behaviour of the PDFs. The DNS results have a PDF which differs by more than an order of magnitude at the exponential wings from the experimental results, and appears to be increasing with Re_λ. Thus, from comparison with DNS results, a low numerical Reynolds number of ≈ 20 appears reasonable, however comparison with experiment gives the numerical Reynolds number significantly higher at approximately 626.
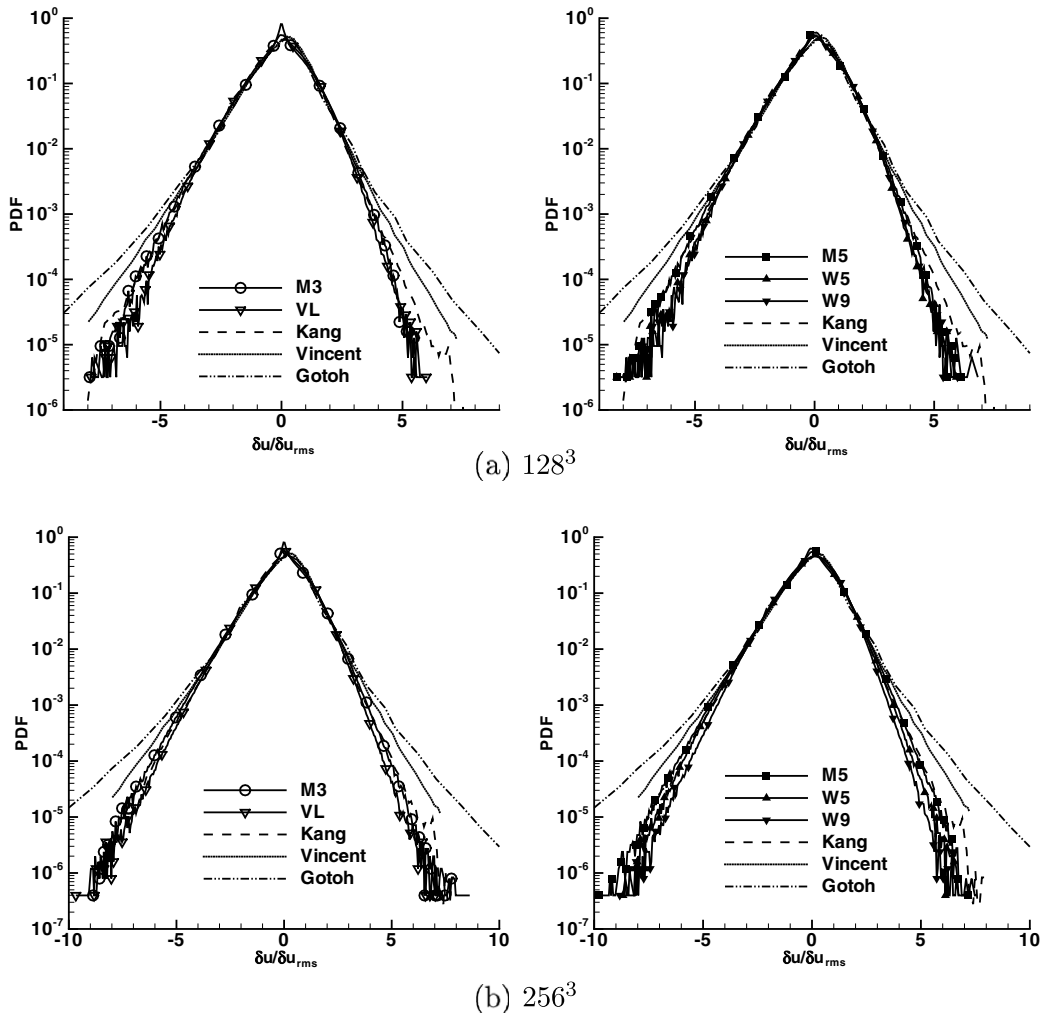
(a) 128^3

(b) 256^3

Fig. 9. Velocity increment PDFs compared to experimental results by Kang et al. [56], and DNS by Vincent and Meneguzzi [73] and Gotoh et al. [74] at $t = 2$.

The pressure PDFs are shown in Fig. 10 for the VL, M5 and W9 schemes at 256^3, where they follow a Gaussian distribution, demonstrating that the pressure is decorrelated from the vorticity. This Gaussian distribution of pressure is found for all schemes at all resolutions. The source of this decorrelation is believed to be the decoupling of pressure and vorticity as described in Section 2.4.

3.5. Spectra

The three-dimensional energy spectrum $E(k)$ is defined as [49]

$$E(k) = 2\pi k^2 \phi_{ii}(k), \tag{51}$$

where $k = \sqrt{k_x^2 + k_y^2 + k_z^2}$ and the spectrum tensor ϕ is

$$\phi_{ij}(\mathbf{k}) = \frac{1}{(2\pi)^3} \int_{-\infty}^{\infty} Q_{ij}(\mathbf{r}) \exp^{-i\mathbf{k}\mathbf{r}} d\mathbf{r}, \tag{52}$$

where Q_{ij} is the second-order velocity correlation tensor. The three-dimensional resolved kinetic energy spectrum for all resolutions and methods at $t = 5$ are shown in Fig. 11 for the second and third-order methods, and
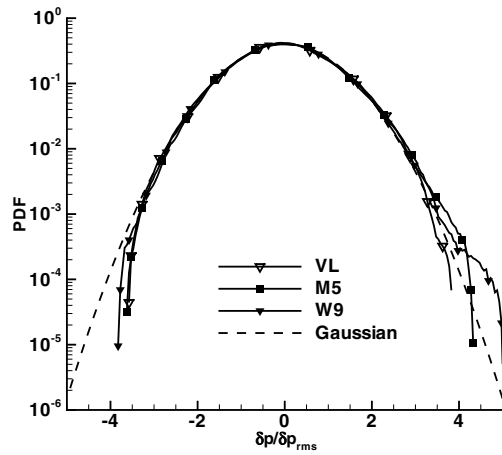
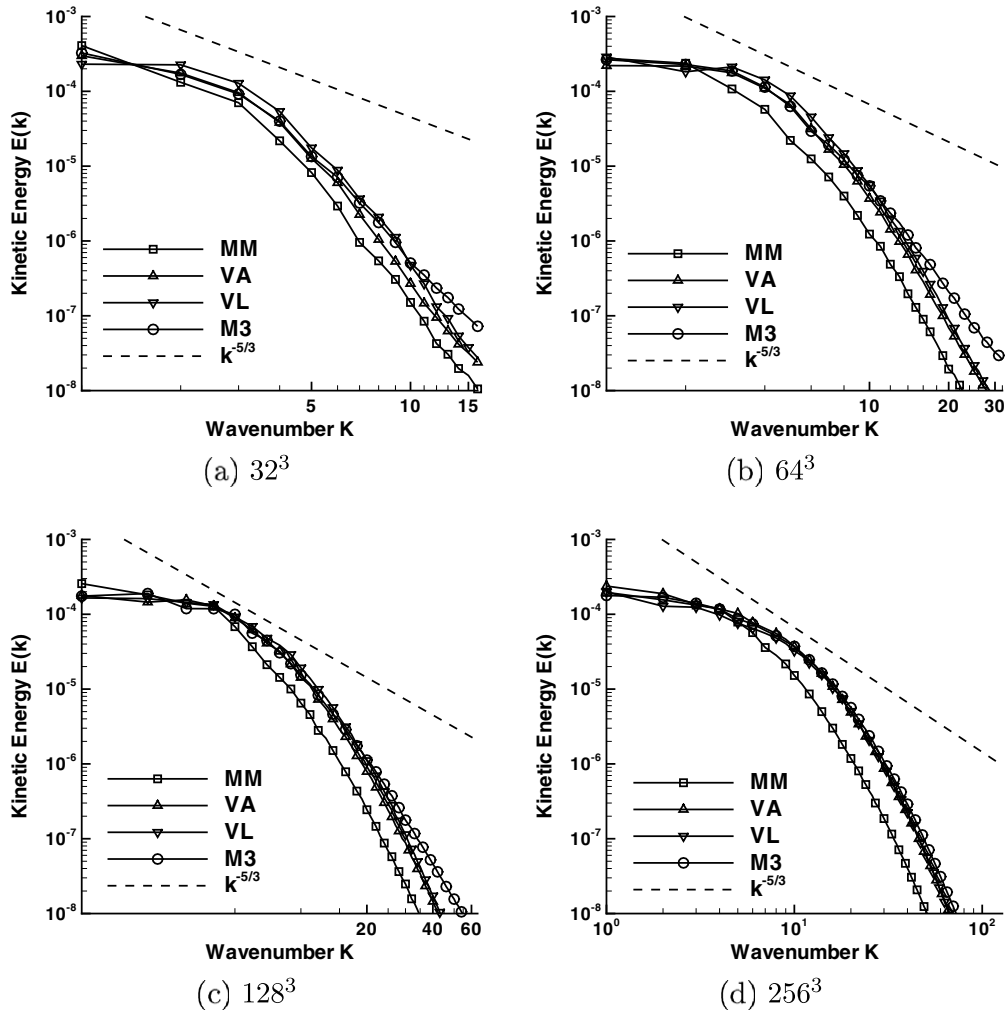Fig. 10. Pressure fluctuation PDF from the 256^3 simulation at $t = 2$.

Fig. 11. Three-dimensional kinetic energy spectrum E_{3D} at $t = 5$ for the second and third-order methods at different resolutions.

in Fig. 12 for the fifth and ninth-order methods. Ideally, the high wave number part of the spectrum should form a straight line in log-log axis with a power law of $k^{-5/3}$ as predicted by Kolmogorov [38]. At 32^3 all limiters except W9 are too dissipative at high wave numbers, leading to lower kinetic energy than ideal. The W9 simulation has a reasonable inertial range to the cutoff. Given that the degrees of freedom within the system are low, this is an excellent result. However, increasing the resolution to 64^3 does not give a corresponding increase in the $k^{-5/3}$ range, although at this resolution there also is a short inertial range in simulations using the fifth-order methods. Interestingly, the M5 method is less dissipative than W5 at high wave numbers, leading to a slightly 'fuller' spectrum.

The trend towards increasing size of the range with approximate Kolmogorov scaling continues for 128^3 and 256^3 for the higher-order schemes, with very little or no inertial range for the second and third-order limiters until the highest resolution. Table 6 details the ratio of the wave number at which the energy spectrum deviates more than 10% from an assumed $k^{-5/3}$ to the maximum wave number k_{max} for the given grid. At the grid resolutions considered, this appears to be reaching a value independent of grid resolution, indicating that the simulations are of a large eddy nature, and not following a constant dissipation Kolmogorov range scaling, where k/k_{max} would decrease with increasing effective Reynolds number [22].

In comparing the schemes, Minmod shows effectively no inertial range, and the data in Table 6 are representative of this. It gives consistently worse resolution of high wave number modes when compared to the
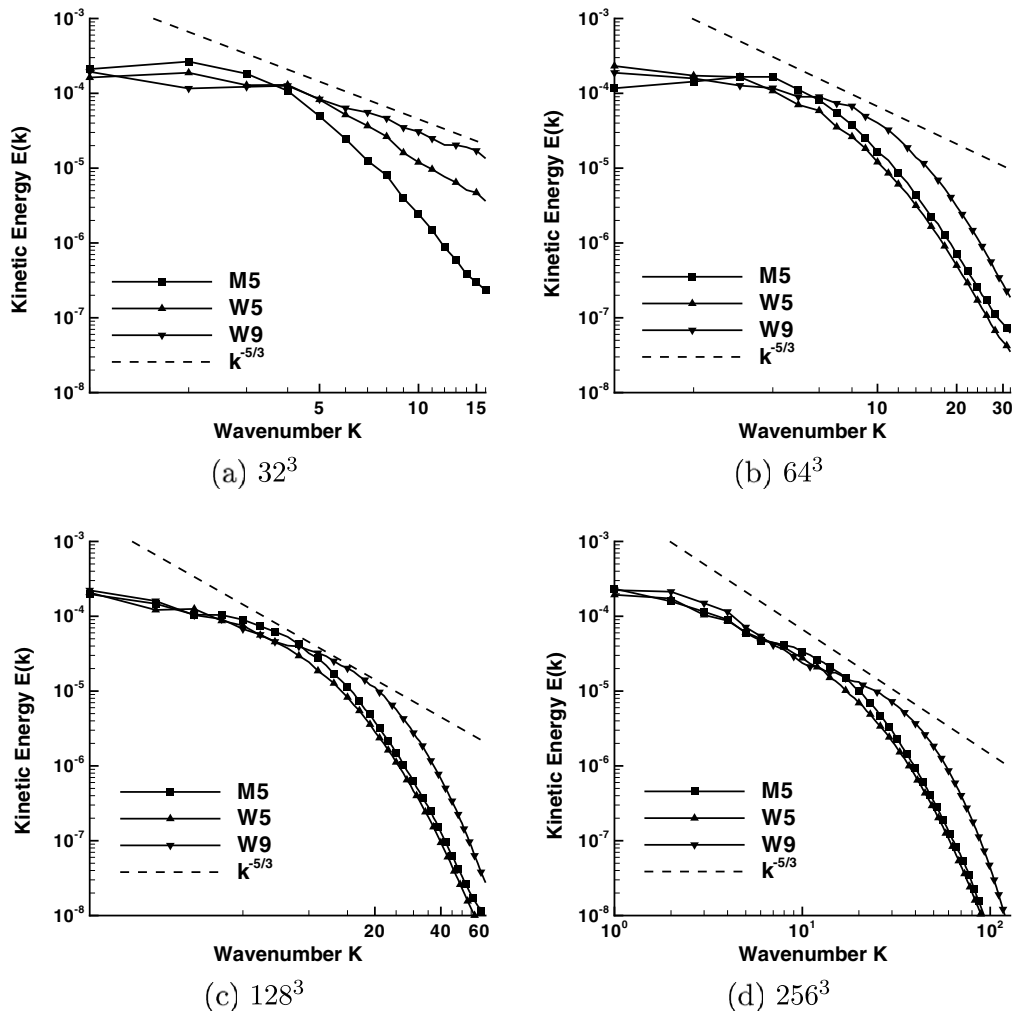

Fig. 12. Three-dimensional kinetic energy spectrum E_{3D} at $t = 5$ for the fifth and ninth-order methods at different resolutions.

Table 6
Highest normalised wave number (k/k_{max}) at which the resolved kinetic energy spectrum deviates more than 10% from an assumed $k^{-5/3}$ law

Resolution	MM	VA	VL	M3	M5	W5	W9
32^3	0.19	0.19	0.19	0.19	0.25	0.31	1.0
64^3	0.09	0.13	0.16	0.13	0.22	0.25	0.34
128^3	0.05	0.10	0.13	0.11	0.19	0.19	0.31
256^3	0.05	0.10	0.10	0.10	0.16	0.16	0.31

other second-order limiters. As stated in Section 2.3 the leading order difference between the limited quantities for MM is second-order, however for VA, VL and M3 the difference is third-order. As the dissipation in a Godunov scheme is proportional to the difference of extrapolated quantities, the lower the leading order of the difference, the higher the dissipation. Examining the spectra in Fig. 11 it is clear that the MM limiter is more dissipative, and that the formally second-order accurate VL and VA methods have behaviour closer to that of the third-order accurate M3. These resolve a short inertial range up to $k_{max}/10$.

Significant improvements are seen at fifth-order where the dissipative ranges begin at $k_{max}/6$ and at ninth-order at $k_{max}/3$. From this it can be seen that using fifth and higher-order methods are comparable to increasing the resolution by a factor of two in each direction when compared to the second and third-order limiters, thus easily justifying the increase in computational time. As turbulent velocities scale as $k^{-1/3}$ then if it is assumed that a $k^{-5/3}$ range exists to the cutoff then even at the maximum grid resolution the smallest eddies still have a mean turbulent velocity one fifth of that at the peak. This is an extremely noisy signal and very difficult to capture accurately using any numerical method in physical space. Results gained here for the higher-order schemes indicate that the simulations capture modes of wavelength of 10 cells with reasonable statistical accuracy, which is considered to be a good result.

The Kolmogorov constant has been computed and it is found that $C_k \approx 1.9$ for the three-dimensional spectrum. This is in good agreement with the 'bump' at the beginning of the sub-inertial range where $C_k \approx 2$, as reported in recent DNS [75,74], and experimental results [76,56,77,54,78], but higher than the theoretical value of $C_k \approx 1.6$ expected. It should be noted that these are single time spectra from decaying turbulence not averaged from statistically stationary forced turbulence.

A further measurement of the presence of a sub-inertial range is by computing Kolmogorov's four-fifth's law. As the problem is not stationary (i.e. it is decaying) the results were calculated from the Karman–Howarth equation for an inviscid fluid, hence including a contribution from the time variation of the second-order structure function [2],

$$-\left[\frac{3}{r^4}\int_0^r s^4\frac{\partial}{\partial t}D_{LL}(s,t)\mathrm{d}s + D_{LLL}(r,t)\right]\Big/\epsilon r = \frac{4}{5} = \mathcal{B}, \tag{53}$$

where $D_{LL} = \overline{[u(x_1 + e_1\frac{4}{5} = r,t) - u(x_1,t)]^2}$, $D_{LLL} = \overline{[u(x_1 + e_1 r,t) - u(x_1,t)]^3}$ and s is a dummy integration variable. In forced turbulence this relationship holds at $Re_\lambda > 1170$ [40], and Antonia and Burattini [79] suggest that for decaying isotropic turbulence the asymptotic value of four-fifths is not reached until $Re_\lambda > 10^6$.

$\mathcal{B}$ is plotted in Fig. 13 at a grid resolution of 256^3 results for the van Leer, M3, M5, and WENO methods. The four-fifths law is not satisfied for any of the methods. Comparing the results with experiment suggest $Re_\lambda < 100$.

The short extent of the sub-inertial range (if present at all) indicates that the ILES approach using standard compressible finite volume methods would not be appropriate for accurate resolution of flow where the features of interest are less than several mesh cells in size.

3.6. Spectral distribution of numerical viscosity

From the previous subsections it appears that the M3, M5 and W9 limiters are the optimum choices compared to schemes of similar order of accuracy. To further quantify the performance of these schemes the spectral behaviour of the numerical viscosity is examined. Garnier et al. [23] computed the amplification factor for
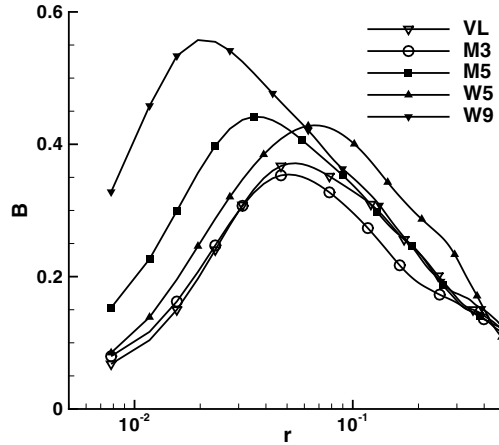
Fig. 13. $\mathcal{B}$ plotted for the 256^3 grid resolution at $t = 5$.

upwind fluxes, showing that a unique filter length cannot be defined for the Euler equations. This will be examined here. Secondly, the numerical viscosity is computed in the form of a numerical spectral eddy viscosity as proposed by Domaradzki et al. [80]. This is compared to the theoretical 'ideal' eddy viscosity for homogeneous decaying turbulence computed by Chollet [81] via the test field model and eddy damped quasi-normal Markovian approximation. This method of comparison has been employed by Hickel et al. [20] to optimise incompressible implicit LES.

Following Garnier et al. [23] the amplification of the fourier modes due to discretisation errors can be computed as the ratio of the Fourier transform of the finite volume fluxes over the spectral fluxes,

$$
\mathcal{A} = \frac{\sum_{k-1/2<|\mathbf{k}|<k+1/2}\text{FFT}|(\partial\mathbf{E}/\partial x + \partial\mathbf{F}/\partial y + \partial\mathbf{G}/\partial z)|^2}{\sum_{k-1/2<|\mathbf{k}|<k+1/2}|ik_1\text{FFT}(\mathbf{E}) + ik_2\ \text{FFT}(\mathbf{F}) + ik_3\text{FFT}(\mathbf{G})|^2}, \tag{54}
$$

which can be rewritten using Eq. (1) as,

$$
\mathcal{A} = \frac{\sum_{k-1/2<|\mathbf{k}|<k+1/2}\text{FFT}| - \partial\mathbf{U}/\partial t|^2}{\sum_{k-1/2<|\mathbf{k}|<k+1/2}|ik_1\text{FFT}(\mathbf{E}) + ik_2\text{FFT}(\mathbf{F}) + ik_3\text{FFT}(\mathbf{G})|^2}. \tag{55}
$$

The numerator is computed as a central difference approximation for the derivative of the conserved variables with respect to time, i.e. $(\mathbf{U}^{n+1} - \mathbf{U}^{n-1})/\Delta t$, and the spectral divergence as a function of the conserved variables at time level n. Fig. 14 shows the ratio of the fluxes computed for the M3, M5 and W9 schemes for 64^3 to 256^3 for the continuity and ρu momentum equation. The results for the energy equation are very similar to those of the continuity equation, and the ρv and ρw momentum equations match the ρu equation.

As shown in [23] the effective filter length is different for the continuity and momentum equations. Increasing the resolution of the numerical scheme does not significantly improve the resolution of the continuity and energy equations, and at the highest resolution there is only a 20% difference in cut-off wave number for $\mathcal{A}_1$ over all methods.

Table 7 details the cut-off filter length, which is defined as the highest wave number for which $\mathcal{A} > 0.9$, normalised by $k_{\max}$. Comparing these to the results in Table 6 it can be seen that for M3 and M5 the cut-off point for the $k^{-5/3}$ range is at lower wave number than the highest effective cut-off wave number for the continuity and energy equation ($\mathcal{A}_1$ and $\mathcal{A}_5$). However, the WENO ninth-order inertial range cut-off lies between the effective filter length for the continuity and momentum equations. The normalised effective filter length appears to be converging to a constant value independent of grid size, being approximately $k_{\max}/5$ for M3, $k_{\max}/3$ for M5 and $k_{\max}/2$ for W9. All three schemes are dissipative, the maximum amplification of a given wave number is 6% for M3, 2.5% for M5 and 0.1% for W9 at 64^3, becoming negligible at higher grid resolutions. This is likely to be due to the accuracy of the central difference approximation of the change in
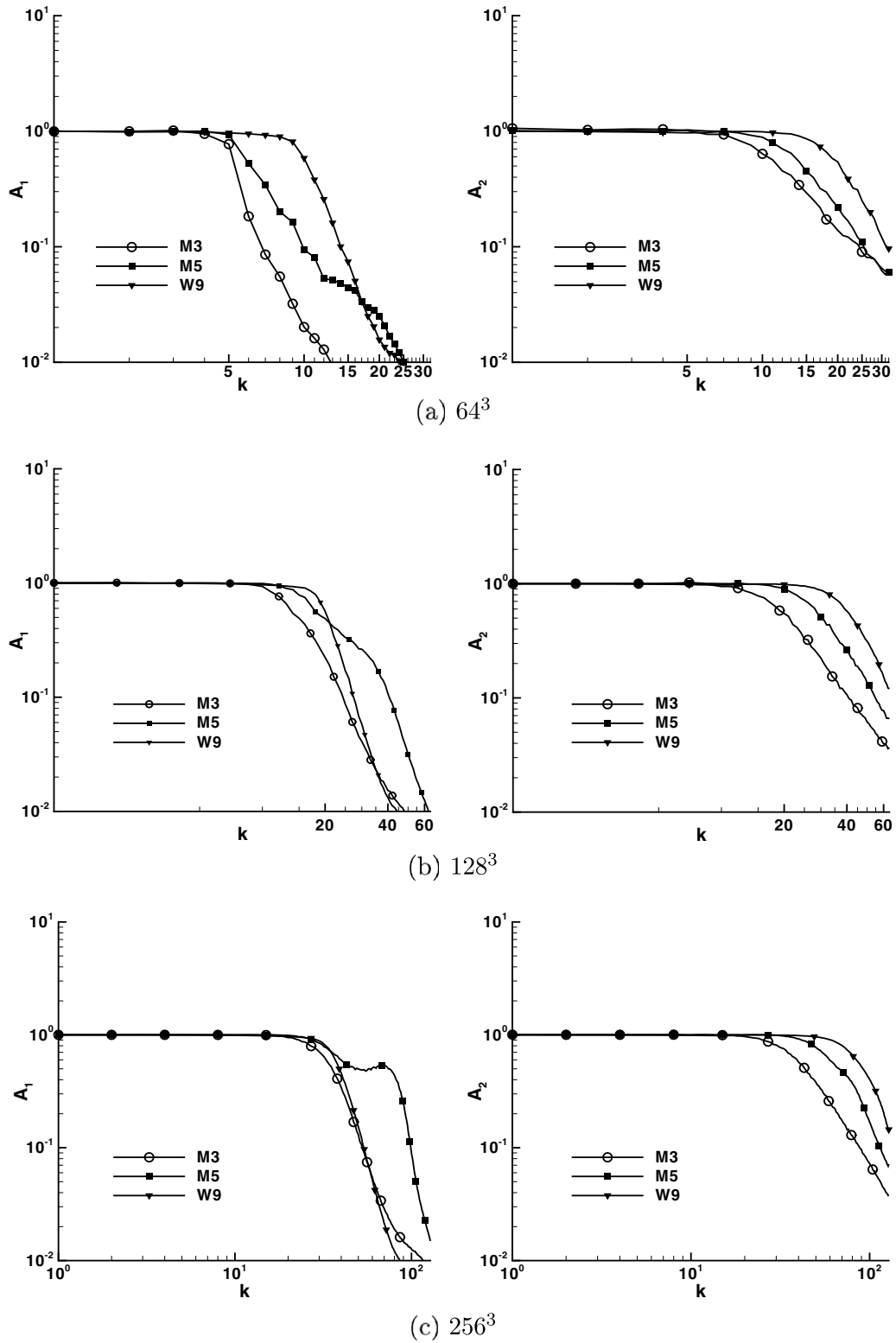
Fig. 14. The ratio of the fluxes computed using the FV schemes to spectral fluxes at $t = 5$ for the continuity equation (left) and u-momentum equation (right).

Table 7
Highest normalised wave number (k/k_{max}) at which $\mathcal{A} > 0.9$

Scheme	64^3		128^3		256^3	
	$\mathcal{A}_1$	$\mathcal{A}_2$	$\mathcal{A}_1$	$\mathcal{A}_2$	$\mathcal{A}_1$	$\mathcal{A}_2$
M3	0.16	0.25	0.17	0.20	0.18	0.20
M5	0.19	0.31	0.19	0.31	0.22	0.33
W9	0.28	0.46	0.28	0.46	0.23	0.48

conserved quantities over the time, hence explaining why the maximum amplification decreases as grid size increases.

Next, the effective numerical viscosity is assessed for it's suitability as a turbulent eddy viscosity. The momentum equations can be written in spectral form as

$$\left(\frac{\partial}{\partial t} + vk^2\right)u_n(\mathbf{k}, t) = -\frac{i}{2}P_{nlm}(\mathbf{k})\int u_l(\mathbf{p}, t)u_m(\mathbf{k} - \mathbf{p}, t)\mathrm{d}^3 p, \tag{56}$$

where the projection tensor is defined as,

$$P_{nlm}(\mathbf{k}) = k_m(\delta_{nl} - k_n k_l/k^2) + k_l(\delta_{nm} - k_n k_m/k^2). \tag{57}$$

The evolution equation for kinetic energy as a function of wave number is derived by multiplying Eq. (56) by $u_n^*(\mathbf{k}, t)$, where * indicates the complex conjugate, giving

$$\frac{\partial \frac{1}{2}|u(\mathbf{k}, t)|^2}{\partial t} = -2vk^2\frac{1}{2}|u(\mathbf{k}, t)|^2 + T(\mathbf{k}, t), \tag{58}$$

$$T(\mathbf{k}, t) = \frac{1}{2}\mathrm{Im}\left[u_n^*(\mathbf{k}, t)P_{nlm}(\mathbf{k})\int u_l(\mathbf{p}, t)u_m(\mathbf{k} - \mathbf{p}, t)\mathrm{d}^3 p\right]. \tag{59}$$

The spectra can be integrated in spherical shells to give the Transfer function $T(k)$ and energy spectrum $E(k)$ as a function of wave vector magnitude k,

$$E(k) = 4\pi k^2\frac{1}{2}\langle|u(\mathbf{k}, t)|^2\rangle, \tag{60}$$

$$T(k) = 4\pi k^2\langle T(\mathbf{k}, t)\rangle. \tag{61}$$

Eq. (58) can be rewritten as

$$\frac{\partial}{\partial t}E(k, t) = -2vk^2 E(k, t) + T(k, t). \tag{62}$$

By assuming that the numerical viscosity behaves in a manner analogous to physical viscosity, an effective numerical viscosity for inviscid simulations can be computed using

$$v_n = \frac{T(k, t) - \frac{\partial}{\partial t}E(k, t)}{2k^2 E(k, t)}, \tag{63}$$

computed numerically as [80]

$$v_n = \frac{T(k, t^n) - (E(k, t^{n+1}) - E(k, t^{n-1}))/2\Delta t}{2k^2 E(k, t^n)}, \tag{64}$$

where modes are included in the computation only if the magnitude of the wave vector is smaller than a cut-off wave number k_c. It is normalised using the energy at the cutoff wave number $E(k_c)$ and k_c

$$v_n^+(k|k_c) = \frac{v_n}{\sqrt{E(k_c)/k_c}}. \tag{65}$$

This is compared to the theoretical result fitted by the expression of Chollet [81]

$$v_n^+(k|k_c) = C_K^{-3/2}(0.441 + 15.2\exp^{-3.03k_c/k}).$$ (66)

The computation of the effective numerical viscosity is quite sensitive to the choice of the cut-off wave number k_c. Plotted in Fig. 15 are the effective numerical viscosities for $k_c = k_{max}/2$. Also plotted are the effective numerical viscosities where k_c is the average of the filter cut-offs measured from $\mathcal{A}(k)$.

At $k/k_c > 0.3$ in all simulations there is a very good qualitative agreement in terms of the shape of the numerical spectral viscosity in comparison to the theoretical curve. Both numerical and theoretical lines have a region of approximately constant viscosity at intermediate wave numbers, and increasing viscosity as $k/k_c \to 1$. The effective dissipation is consistent with the previous results, showing the W9 scheme as the least dissipative, and M3 as the most dissipative. At the cut-off wave numbers chosen here the effective viscosity of the W9 scheme is lower than the ideal spectral eddy viscosity, which implies that the scheme could benefit from the addition of a sub-grid model. However, if a higher wave number cut-off is chosen, the effective numerical viscosity increases above the theoretical line.

The agreement with the theoretical results of Chollet is reasonable, however, when employing the effective cut-off from $\mathcal{A}(k)$, the number of modes between the energy containing modes (approximately $1 < k < 5$) and
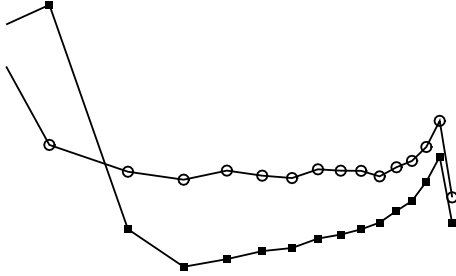
the cut-off is very low, even for ninth-order methods at 128^3. This can be seen in Fig. 15, where each symbol represents a mode. At 64^3 each method has less than 10 wave numbers in this range, at 128^3 less than 20.

These results imply that given a high enough grid resolution it is possible to select a cut-off wave number for each method which gives a spectral viscosity in agreement with Chollet's theory. The key issue at present is that the required grid resolution is prohibitively large for many practical situations of industrial interest.

At low wave numbers the effective numerical viscosity becomes negative for some wave numbers, positive for others, and increases in magnitude. This increase in effective viscosity can also be seen in Ciardi et al. [82]. It is interesting that for some modes the effective viscosity becomes negative. This occurs for modes where the net transfer of kinetic energy ($T(k)$) is negative, yet the turbulent kinetic energy at that mode increases. As all schemes have been shown to be dissipative at all modes on average (Fig. 14), it is possible that this is due to compressibility effects as discussed in Section 2.4. There can be an increase in kinetic energy at some points in the flow due to a local exchange of energy from pressure to kinetic energy in the acoustic modes. When there are statistically few modes (i.e. at low wave numbers) this local exchange could cause an increase in total turbulent kinetic energy at a given wave number. This is not taken into account in Eq. (58) as this expression is valid only for incompressible flows.

4. Conclusions

The ability of high-order finite volume Godunov-type ILES schemes to simulate isotropic, homogeneous decaying turbulence at low Mach number has been investigated quantitatively using a number of different parameters. The homogeneous isotropic flow field is initialised using the divergence of a vector potential to minimise the compressible component of the kinetic energy spectrum.

It has been demonstrated that the behaviour of the large scales is captured well at resolutions greater than 32^3, or when using numerical methods of higher than third-order accuracy. With this constraint satisfied the turbulent kinetic energy decay exponent lies close to the theoretical and experimental results, and is as accurate as results reported for conventional large eddy simulation. The integral length scale is expected to grow as $t^{2/7}$ for the initialised energy spectrum, and this is shown to hold for all methods. Additionally, velocity increment PDFs are found to have exponential wings, but pressure PDFs are essentially Gaussain.

Examining the spectra indicate that all methods are too dissipative at high wave numbers, giving a slope steeper than the expected $k^{-5/3}$, and there is no agreement with the Kolmogorov four-fifths law. All methods have effective filters at less than $k_{\max}/2$ for the momentum equations and $k_{\max}/4$ for the continuity and energy equation, indicating that a single filter length cannot be defined for all equations. When the numerical viscosity is assessed as a spectral eddy viscosity it is in good qualitative agreement with the theoretical solution, having a plateau at intermediate wave numbers and a peak at the cut off. However, unless the cut-off wave number is chosen below $k_{\max}/2$ then all methods are too dissipative.

It is difficult to define a single effective Reynolds number for the simulations. Comparing the PDF's to experimental results gives an estimated $Re_\lambda \approx 600$, however, compared to DNS it is an order of magnitude lower. Examining the four-fifths law shows $Re_\lambda \approx 30$–100 for all methods except WENO ninth-order which is approximately 200.

In comparing the numerical methods, the fifth and ninth-order methods have a clear advantage in that they are capable of resolving non-Gaussian turbulent behaviour at lower resolutions than the second and third-order methods. Of the second and third-order methods the third-order limiter M3 performs the best - giving a velocity derivative skewness close to experimental for all resolutions greater than 32^3 whilst maintaining a reasonable kinetic energy decay rate. Additionally, the third-order limiter has marginally higher kinetic energy at the high wave numbers, and gives a better match to experimental velocity increment PDFs. Considering computational time, however, the complexity of this limiter would make it undesirable as it is more expensive than the fifth-order methods.

Of the very high-order methods, plots of enstrophy show that using a ninth-order scheme gives a similar solution to the second and third-order methods at double the resolution. The two fifth-order schemes give a solution marginally less than double. This is confirmed by calculating the effective numerical filter length, where the WENO ninth-order method resolves double the wave numbers of the M3 method. Interestingly,

there is only a marginal improvement in resolution of the energy and continuity equation at the higher grid sizes. The M5 limiter gives excellent agreement with experimental results in predicting the intermittency in the tails of the velocity increment PDFs, whereas the WENO methods drop off steeply at the tails. Examining the kinetic energy spectra shows that the ninth-order method resolves an approximate $k^{-5/3}$ to $k_{max}/3$, the fifth-order method up to $k_{max}/6$, and lower-order methods up to $k_{max}/10$. This means that fifth and higher-order methods at 128^3 perform better than the second-order methods at 256^3. The increase in accuracy via this measure is greater than the increase in computational time.

In summary, the numerical methods ranked in order of decreasing performance with respect to accuracy for a given computational time are WENO ninth-order, followed by MUSCL fifth-order, WENO fifth-order, MUSCL third-order, van Leer, van Albada and Minmod. For a given simulation it is expected that an optimum choice would be either WENO ninth-order or MUSCL fifth-order depending on the monotonicity constraints of a given problem.

Future work in this area is focussed on the simulation of Rayleigh–Taylor and Richtmyer–Meshkov instabilities in mixing layers between two miscible fluids. In this case the transition from a perturbed interface to a fully developed flow field has not been fully characterised and requires high resolution numerical methods capable of resolving the laminar growth of a small perturbation through to a fully developed flow field. Additionally, there is ongoing work on understanding the role of the increase of entropy in the solution of the Riemann problem leading to irreversible dissipation of kinetic energy.

Acknowledgements

Appendix A. Symmetric limiters

The MUSCL (monotone upstream-centred schemes for conservation laws) method is used to determine the cell interface variables by extrapolating the cell averaged variables. Examing Eq. (9) it is clear that if

$$\phi(r^L)(U_i - U_{i-1}) = \phi\left(\frac{1}{r^L}\right)(U_{i+1} - U_i), \tag{A.1}$$

$$\phi(r^R)(U_i - U_{i-1}) = \phi\left(\frac{1}{r^R}\right)(U_{i+1} - U_i), \tag{A.2}$$

then the resultant interpolated quantity is independent of k. This is the case for the van Albada, van Leer and Minmod limiters which are always of second-order accuracy in the standard MUSCL format. As an example this can be shown to be true for the van Leer limiter. Setting the differences $(U_i - U_{i-1}) = \Delta_{i-1/2}$ and $(U_{i+1} - U_i) = \Delta_{i+1/2}$, then the left-hand interpolated values are independent of k as

$$\phi(r^L)(U_i - U_{i-1}) = \frac{2r^L}{1 + r^L}(U_i - U_{i-1}), = \frac{2\Delta_{i+1/2}\Delta_{i-1/2}}{\Delta_{i-1/2}(1 + \Delta_{i+1/2}/\Delta_{i-1/2})}, = \frac{2\Delta_{i+1/2}\Delta_{i-1/2}}{\Delta_{i-1/2} + \Delta_{i+1/2}}, \tag{A.3}$$

also,

$$\phi\left(\frac{1}{r^L}\right)(U_{i+1} - U_i) = \frac{2/r^L}{1 + 1/r^L}(U_{i+1} - U_i), = \frac{2\Delta_{i-1/2}\Delta_{i+1/2}}{\Delta_{i+1/2}(1 + \Delta_{i-1/2}/\Delta_{i+1/2})}, = \frac{2\Delta_{i+1/2}\Delta_{i-1/2}}{\Delta_{i-1/2} + \Delta_{i+1/2}}. \tag{A.4}$$

thus demonstrating that this limiter satisfies the criteria in Eq. (A.2) meaning that it is at most second-order accurate. Equivalent results can be shown for the Minmod, van Albada and other second-order limiters.

References

[1] M. Lesieur, O. Metais, New trends in large-eddy simulations of turbulence, Annu. Rev. Fluid Mech. 28 (1996) 45–82.

[2] S. Pope, Turbulent Flows, Cambridge University Press, 2000.

[3] D. Drikakis, Advances in turbulent flow computations using high-resolution methods, Prog. Aerosp. Sci. 39 (2003) 405–424.

[4] D. Drikakis, W. Rider, High-resolution Methods for Incompressible and Low-speed Flows, Springer Verlag, 2004.

[5] F. Grinstein, L. Margolin, W. Rider (Eds.), Implicit large eddy simulation, Computing Turbulent Fluid Dynamics, Cambridge University Press, 2007.

[6] P. Sagaut, Large Eddy Simulation for Incompressible Flows, Springer Verlag, 2001.

[7] D. Youngs, Application of miles to Rayleigh–Taylor and Richtmyer–Meshkov Mixing, AIAA-2003-4102.

[8] D. Youngs, Three-dimensional numerical simulation of turbulent mixing by Rayleigh–Taylor instability, Phys. Fluids A 3 (5) (1991) 1312–1320.

[9] J. Boris, F. Grinstein, E. Oran, R. Kolbe, New insights into large eddy simulation, Fluid Dyn. Res. 10 (1992) 199–228.

[10] F. Grinstein, C. Fureby, Recent progress on miles for high Reynolds number flows, J. Fluid Eng. – Trans. ASME 848 (2002) 848–861.

[11] M. Hahn, D. Drikakis, Large eddy simulation of compressible turbulence using high-resolution method, Int. J. Numer. Meth. Fl. 49 (2005) 971–977.

[12] L. Margolin, P. Smolarkiewicz, Z. Sorbjan, Large-eddy simulations of convective boundary layers using nonoscillatory differencing, Physica D 133 (1999) 390–397.

[13] P. Smolarkiewicz, L. Margolin, Mpdata: a finite difference solver for geophysical flows, J. Comput. Phys. 140 (2) (1998) 459–480.

[14] R. Gordnier, M. Visbal, Compact different scheme applied to simulation of low-sweep delta wing flow, AIAA J. 43 (8) (2005) 1744–1752.

[15] D. Drikakis, C. Fureby, F. Grinstein, M. Hahn, D. Youngs, Miles of transition to turbulence in the Taylor–Green vortex system, in: ERCOFTAC Workshop on Direct and Large Eddy Simulation-6, 2006, p. 133.

[16] C. Fureby, F. Tabor, H. Weller, A. Gosman, A comparative study of subgrid scale models in homogeneous isotropic turbulence, Phys. Fluids 9 (5) (1997) 1416–1429.

[17] D. Porter, P. Woodward, A. Pouquet, Inertial range structures in decaying compressible turbulent flows, Phys. Fluids 10 (1) (1998) 237–245.

[18] C. Fureby, F. Grinstein, Large eddy simulation of high-Reynolds-number free and wall-bounded flows, J. Comput. Phys. 181 (2002) 68–97.

[19] L. Margolin, P. Smolarkiewicz, A. Wyszogrodzki, Implicit turbulence modelling for high Reynolds number flows, J. Fluids Eng. 124 (2002) 862–867.

[20] S. Hickel, N. Adams, J. Domaradzki, An adaptive local deconvolution method for implicit les, J. Comput. Phys. 213 (2006) 413–436.

[21] L. Margolin, W. Rider, F. Grinstein, Modeling turbulent flow with implicit les, J. Turbul. 7 (15) (2006) 1–27.

[22] J. Hinze, Turbulence, second ed., McGraw-Hill, 1975.

[23] E. Garnier, M. Mossi, P. Sagaut, P. Comte, M. Deville, On the use of shock-capturing schemes for large-eddy simulation, J. Comput. Phys. 153 (1999) 273–311.

[24] A. Eberle, Characteristic flux averaging approach to the solution of euler's equations, Technical Report, VKI Lecture Series, 1987.

[25] S. Gottlieb, C.-W. Shu, Total variation diminishing Runge–Kutta schemes, Math. Comput. 67 (221) (1998) 73–85.

[26] B. van Leer, Towards the ultimate conservative difference scheme.iv. a new approach to numerical convection, J. Comput. Phys. 23 (1977) 276–299.

[27] D. Balsara, C.-W. Shu, Monotonicity preserving weighted essentially non-oscillatory schemes with increasingly high order of accuracy, J. Comput. Phys. 160 (2000) 405–452.

[28] E. Toro, Riemann Solvers and Numerical Methods for Fluid Dynamics, Springer-Verlag, 1997.

[29] K. Kim, C. Kim, Accurate, efficient and monotonic numerical methods for multi-dimensional compressible flows part ii: Multi-dimensional limiting process, J. Comput. Phys. 208 (2005) 570–615.

[30] J. Zoltak, D. Drikakis, Hybrid upwind methods for the simulation of unsteady shock-wave diffraction over a cylinder, Comput. Method Appl. M 162 (1998) 165–185.

[31] C.-W. Shu, S. Osher, Efficient implementation of essentially non-oscillating shock-capturing schemes, J. Comput. Phys. 77 (1988) 439–471.

[32] C.-W. Shu, S. Osher, Efficient implementation of essentially non-oscillating shock-capturing schemes II, J. Comput. Phys. 83 (1989) 32–78.

[33] G.-S. Jiang, C.-W. Shu, Efficient implementation of weighted ENO schemes, J. Comput. Phys. 126 (1996) 202–228.

[34] A. Harten, B. Engquist, S. Osher, S. Chakravarthy, Uniformly high order accurate essentially non-oscillatory schemes, iii, J. Comput. Phys. 71 (2) (1987) 231–303.

[35] L. Margolin, W. Rider, The design and construction of implicit les modes, Int. J. Numer. Meth. Fl. 47 (2005) 1173–1179.

[36] D. Carati, G. Winckelmans, H. Jeanmart, Exact expansions for filtered-scales modelling with a wide class of les filters, in: Direct and Large Eddy Simulation III, Kluwer, 1999, pp. 213–224.

[37] L. Margolin, W. Rider, A rationale for implicit turbulence modelling, Int. J. Numer. Meth. Fl. 39 (2002) 821–841.

[38] A. Kolmogorov, The local structure of turbulence in an incompressible fluid at very high Reynolds numbers, Dokl. Akad. Nauk. SSSR 30 (1941) 299.

[39] A. Kolmogorov, A refinement of previous hypotheses concerning the local structure of turbulence in a viscous incompressible fluid at high Reynolds number, J. Fluid Mech. 13 (1962) 82–85.

[40] F. Moisy, P. Tabeling, H. Willaime, Kolmogorov equation in a fully developed turbulence experiment, Phys. Rev. Lett. 82 (20) (1999) 3994–3997.

[41] H. Bethe, On the theory of shock waves for an arbitrary equation of state, Technical Report, Office of Scientific Research and Development, May 1942.

[42] J. Johnson, R. Cheret (Eds.), Classic Papers in Shock Compression Science, Springer-Verlag, 1998.

[43] B. Thornber, D. Drikakis, R. Williams, The dissipation of kinetic energy within Godunov schemes I: theoretical analysis, J. Comput. Phys. (submitted for publication).

[44] G. Blaisdell, N. Mansour, W. Reynolds, Compressibility effects on the growth and structure of homogeneous turbulent shear flow, J. Fluid Mech. 256 (1993) 443–485.

[45] G. Erlebacher, M. Hussaini, H. Kreiss, S. Sarkar, The analysis and simulation of compressible turbulence, Theor. Comp. Fluid Dyn. 2 (1990) 73–95.

[46] R. Samtaney, D. Pullin, B. Kosovic, Direct numerical simulation of decaying compressible turbulence and shocklet statistics, Phys. Fluids 13 (5) (2001) 1415–1430.

[47] A. Simone, G. Coleman, C. Cambon, The effect of compressibility on turbulent shear flow: a rapid distortion theory and direct numerical simulation study, J. Fluid Mech. 330 (1997) 307–338.

[48] L. Kovasznay, Turbulence in supersonic flow, J. Aero. Sci. 20 (1953) 657–682.

[49] P. Davidson, Turbulence - An Introduction for Scientists and Engineers, Oxford University Press, 2004.

[50] H. Tennekes, J. Lumley, A First Course in Turbulence, MIT Press, 1972.

[51] M. Oberlack, On the decay exponent of isotropic turbulence, Proc. Appl. Math. Mech. 1 (2002) 294–297.

[52] G. Comte-Bellot, S. Corrsin, The use of a contraction to improve the isotropy of grid generated turbulence, J. Fluid Mech. 25 (1966) 657–682.

[53] M. Mohammed, J. LaRue, The decay power law in grid-generated turbulence, J. Fluid Mech. 219 (1990) 195–215.

[54] Z. Mydlarski, L. Warhaft, On the onset of high-Reynolds grid-generated wind tunnel turbulence, J. Fluid Mech. 320 (1996) 331–368.

[55] L. Skrbek, S. Stalp, On the decay of homogeneous isotropic turbulence, Phys. Fluids 12 (8) (2000) 1997–2019.

[56] H. Kang, S. Chester, C. Meneveau, Decaying turbulence in an active-grid-generated flow and comparisons with large-eddy simulation, J. Fluid Mech. 480 (2003) 129–160.

[57] G. Birkhoff, Fourier synthesis of homogeneous turbulence, Commun. Pure Appl. Math. 7 (1954) 19–44.

[58] M. Lesieur, Turbulence in Fluids, Kluwer Academic Publishers, 1987.

[59] V. Yakhot, S. Orszag, Renormalization group analysis of turbulence, Phys. Rev. Lett. 57 (1986) 1722–1725.

[60] V. Yakhot, Decay of three-dimensional turbulence at high Reynolds numbers, J. Fluid Mech. 505 (2004) 87–91.

[61] T. Ishida, P. Davidson, Y. Kaneda, On the decay of isotropic turbulence, J. Fluid Mech. 564 (2006) 455–475.

[62] O. Metais, M. Lesieur, Spectral large-eddy simulation of isotropic and stably stratified turbulence, J. Fluid Mech. 239 (1992) 157–194.

[63] D. Carati, S. Ghosal, P. Moin, On the representation of backscatter in dynamic localization models, Phys. Fluids 7 (3) (1995) 606–616.

[64] L. Wang, S. Chen, J. Brasseur, J. Wyngaard, Examination of hypotheses in the kolmogorov refined turbulence theory through high-resolution simulations. part1. velocity field, J. Fluid Mech. 309 (1996) 113–156.

[65] R. Anderson, C. Meneveau, Effects of the similarity model in finite-difference les of isotropic turbulence using a lagrangian dynamic mixed model, Flow Turbul. Combust. 62 (1999) 201–225.

[66] T. Hughes, L. Mazzei, A. Oberai, The multiscale formation of large eddy simulation: Decay of homogeneous isotropic turbulence, Phys. Fluids 13 (2) (2001) 505–512.

[67] M. Terracol, P. Sagaut, A multilevel-based dynamic approach for subgrid-scale modeling in large-eddy simulation, Phys. Fluids 15 (12) (2003) 3671–3682.

[68] N. Haughen, A. Brandenburg, Inertial range scaling in numerical turbulence with hyperviscosity, Phys. Rev. E 70 (2004) 026405.

[69] S. Chumakov, C. Rutland, Dynamic structure subgrid-scale models for large eddy simulation, Int. J. Numer. Meth. Fl. 47 (2005) 911–923.

[70] M. Brachet, Direct simulation of three-dimensional turbulence in the Taylor–Green vortex, Fluid. Dyn. Res. 8 (1991) 1–8.

[71] K. Sreenivasan, R. Antonia, The phenomenology of small-scale turbulence, Annu. Rev. Fluid Mech. 29 (1997) 435–472.

[72] J. Herring, R. Kerr, Development of enstrophy and spectra in numerical turbulence, Phys. Fluids A 5 (11) (1993) 2792–2798.

[73] A. Vincent, M. Meneguzzi, The spatial structure and statistical properties of homogeneous turbulence, J. Fluid Mech. 225 (1991) 1–20.

[74] T. Gotoh, D. Fukayama, T. Nakano, Velocity field statistics in homogeneous steady turbulence obtained using a high resolution direct numerical simulation, Phys. Fluids 14 (3) (2002) 1065–1081.

[75] Y. Kaneda, T. Ishihara, M. Yokokawa, K. Itakura, A. Uno, Energy dissipation rate and energy spectrum in high resolution direct numerical simulations of turbulence in a periodic box, Phys. Fluids 15 (2) (2003) L21–L24.

[76] K. Sreenivasan, On the universality of the kolmogorov constant, Phys. Fluids 7 (11) (1995) 2778–2784.

[77] S. Saddoughi, S. Veeravalli, Local isotropy in turbulent boundary layers at high Reynolds number, J. Fluid Mech. 268 (1994) 333–372.

[78] S. Cerutti, C. Meneveau, Statistics of filtered velocity in grid and wake turbulence, Phys. Fluids 12 (5) (2000) 1143–1165.

[79] R. Antonia, P. Burattini, Approach to the 4/5 law in homogeneous isotropic turbulence, J. Fluid Mech. 550 (2006) 175–184.
[80] J. Domaradzki, Z. Xiao, P. Smolarkiewicz, Effective eddy viscosities in implicit large eddy simulations of turbulent flows, Phys. Fluids 15 (12) (2003) 3890–3893.
[81] J. Chollet, Turbulent Shear Flows IV, Springer-Verlag, 1984, pp. 62–72 (Chapter: Two-point closures as a subgrid-scale modelling tool for large eddy simulations).
[82] M. Ciardi, P. Sagaut, M. Klein, W. Dawes, A dynamic finite volume scheme for large-eddy simulation on unstructured grids, J. Comput. Phys. 210 (2005) 632–655.
[83] S. Orzag, G. Patterson, Numerical simulation of three-dimensional homogeneous isotropic turbulence, Phys. Rev. Lett. 28 (1972) 76–79.
[84] R. Kerr, Higher order derivative correlations and the alignment of small scale structures in isotropic turbulence, J. Fluid Mech. 153 (1985) 31–58.
[85] R. Panda, V. Sonnad, E. Clementi, Turbulence in a randomly stirred fluid, Phys. Fluids A 1 (6) (1989) 1045–1053.
[86] S. Chen, G. Doolen, R. Kraichnan, Z.-S. She, On statistical correlations between velocity increments and locally averaged dissipation in homogeneous turbulence, Phys. Fluids A 5 (2) (1992) 458–463.
[87] J. Jimenez, A. Wray, P. Saffman, R. Rogallo, The structure of intense vorticity in isotropic turbulence, J. Fluid Mech. 255 (1993) 65–90.